

A Neurodynamic model of Saliency prediction in V1

David Berga , and Xavier Otazu 

Abstract—Computations in the primary visual cortex (area V1 or striate cortex) have long been hypothesized to be responsible, among several visual processing mechanisms, of bottom-up visual attention (also named saliency). In order to validate this hypothesis, images from eye tracking datasets are processed with a biologically plausible model of V1 able to reproduce other visual processes such as brightness, chromatic induction and visual discomfort. Following Li’s neurodynamic model, we define V1’s lateral connections with a network of firing rate neurons, sensitive to visual features such as brightness, color, orientation and scale. The resulting saliency maps are generated from the model output, representing the neuronal activity of V1 projections towards brain areas involved in eye movement control. Our predictions are supported with eye tracking experimentation and results show an improvement with respect to previous models as well as consistency with human psychophysics. We propose a unified computational architecture of the primary visual cortex that models several visual processes without applying any type of training or optimization and keeping the same parametrization.

Index Terms—Saliency, neurodynamic, network, biologically plausible, firing rate, attention, visual cortex, DWT, FNN, V1.

I. INTRODUCTION

VISUAL salience can be defined as “the distinct subjective perceptual quality which makes some items in the world stand out from their neighbors and immediately grab our attention” [32]. In order to understand how visual information is predominantly selected for controlling eye movements, several studies proposed different approaches. Koch and Ullman [35] propose a computational framework in which visual features are integrated to generate a saliency map. These visual features are projected to V1 and later processed distinctively on the ventral (“what”) and dorsal (“where”) streams. These connections are projected to the superior colliculus (SC), which would generate either top-down (relevance) or bottom-up (saliency) control of eye movements by combining neuronal activity from distinct brain areas to a unique map (priority map) [22][79]. Given these distinct levels of processing from the human visual system (HVS), a set of computational models are proposed in order to reproduce eye movement behavior. Itti et al. introduce a biologically-inspired model [33] in which low-level features are extracted using linear DoG filters, their conspicuity is calculated using center-surround differences (inspired by V1’s simple cell computations) and integrated

(pooled to the SC as a master saliency map) using winner-take-all (WTA) mechanisms. Although computations of existing saliency models seem to mimic HVS mechanisms, complexity of scenes make eye-movement behavior hard to predict. Bruce & Tsotsos model [10] offered a semi-supervised mechanism to account for relevant information of the scenes in combination with the bottom-up computations of V1, predicting eye movement behavior at distinct scene contexts. Given the basis of these models, a myriad of computational models, both with artificial and biological inspiration [34][5][85][63], have implemented distinct ways to predict human eye movements obtaining better performance on its predictions [62][7][8][12]. Whether proposed computational eye movement prediction models precisely resemble eye-tracking data, it is questionable to consider that these predictions accurately and specifically represent saliency [9][3].

Li’s work [42][43][44][87] proposes that V1’s computations are the ones responsible of the representation of the aforementioned saliency map. Following her work, the role for the early processing of the visual features relies in V1, which projects to the SC in order to generate bottom-up saccadic eye movements [65][66, Chapter 9][80], mainly driven for this case by uniquely processing low-level visual features. In previous studies [58][15][60], we show that the proposed firing-rate neurodynamic model of V1’s intra-cortical interactions is able to reproduce brightness and color induction effects (as if V1 acted for such as a contrast enhancement mechanism) as well as visual discomfort mechanisms. We aim to use this exact model in order to compute feature conspicuity (distinctiveness between feature maps), which will alternatively represent the function of the aforementioned saliency map. In this study we will demonstrate that the computations for our model are able to reproduce eye movement behavior using eye-tracking experimentation with a trend to acquire state-of-the-art results in comparison to other saliency models as well as to be consistent with psychophysical measurements of saliency.

Reproducing other visual effects

Brightness induction refers to the changes in perceived brightness of a visual target due to the luminance of its surrounding area. From this statement, the HVS can either perceive the visual target and the surrounding area with similar/equal brightness (assimilation) or to perceive brightness differences (contrast). We can observe in Fig. 1A how two grey patches are perceived distinctively whilst being with same brightness.

Similarly, the HVS perceives the chromatic properties of a visual target distinctively depending on the chromaticities

D. Berga and X. Otazu are from the Computer Vision Center and the Department of Computer Science, Autonomous University of Barcelona, Spain (e-mail: dberga@cvc.uab.es).

This work was funded by the Spanish Ministry of Economy and Competitiveness (DPI2017-89867-C2-1-R), Agencia de Gestió d’Ajuts Universitaris i de Recerca (AGAUR) (2017-SGR-649), and CERCA Programme / Generalitat de Catalunya.

of its surrounding area. This phenomena is named chromatic induction. It appears in both “I” and “s” opponent channels (“I” for red-green and “s” for blue-yellow). This effect is observable on Fig. 1B, where the central ring from the reference stimulus (left) appears to be “greener” (being perceived with lower “I” chromatic properties) than the central ring from the test (right), which appears to be “bluer” instead (being perceived with higher “s” chromatic properties).

These effects were reproduced previously in a multiresolution wavelet framework with BiWaM [55] and CiWaM [54] computational models. These models’ aim was to mimic V1’s simple cell mechanisms by computing center-surround differences at distinct color and luminance opponencies. Being inspired by the aforementioned models, Penacchio et al. [58] modeled an excitatory and inhibitory model of V1 as a more biologically plausible approach to solve these problems. Considering V1 physiological and neurodynamic properties of V1 cells [42] at different spatial frequencies and orientations, it is possible to reproduce psychophysical experiments of brightness [58] and chromatic [15] induction effects.

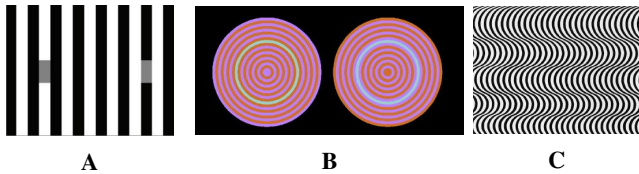


Fig. 1: (A) Brightness induction from the White effect [82]. (B) Chromatic induction from Monnier & Shevell’s concentric ring stimuli [47]. (C) Discomfortable image, credit by Nicholas Wade [77].

Latest experiments showed that our model is also able to predict visual discomfort [60]. Specific visual patterns (Fig. 1C) are shown to cause discomfort, malaise, nausea or even migraine [59][38]. Taking into account the relative contrast energy from stimulus regions (due to its orientation, luminance, chromatic and spatial frequency distributions), we can predict whether a stimulus can cause hyperexcitability in V1, a possible cause of visual discomfort for certain images.

II. MODEL DESCRIPTION

The model is extended from previous implementation by Pennacchio et al. [58] in Matlab and C++¹. Here we describe the main steps in relation to the computations done to the images: II-A. Feature Extraction, II-B. Feature Conspicuity and II-C. Feature Integration. In this section, computations in the early visual pathways will be represented in line with a stimulus example. Overall model architecture was inspired by previous work from Murray et al.’s Saliency WAvelet Model (SWAM), also named Saliency Induction Model (SIM) [48], defining a biologically-inspired and unsupervised low-level model for saliency prediction. Although it provided a promising approach for predicting saliency maps, we aim to highlight novel computations of firing rate dynamics in accordance with physiological properties of V1 cells.

¹Code can be downloaded from <https://github.com/dberga/NSWAM>

A. From images to Sensory Signals: Feature Extraction

1) *Color representation:* Human retinal cone photoreceptors are sensitive to distinct wavelengths of the visual spectrum, corresponding to long (L), medium (M) and short (S) wavelengths. Similarly, traditional digital cameras capture light as values in the RGB color space (corresponding to Red, Green and Blue components). Retinal ganglion cells (RGC) process luminance and chromatic signals as an opponent process. This opponent process separates channels of “Red vs Green” and “Blue vs Yellow” from cone cell responses, and luminance (“Bright vs Dark”) from rod responses. Activity from these channels (R-G, B-Y and L) is then projected respectively to the lateral geniculate nucleus (LGN) as parvo-cellular (P), konio-cellular (K) and magno-cellular (M) pathways towards V1. Likewise, the CIE $L^*a^*b^*$ [4][41] is a color space that defines an opponent color space. We can interpret L^* , a^* and b^* components defined in Eqs. 1,2,3 as means of representing the R-G, B-Y and L opponencies. In Fig. 2 we illustrate an example of an image and its conversion to the *Lab* space, with higher activation on the “Red vs Green” opponent cells than the case of “Blue vs Yellow” and “Bright vs Dark” opponencies.

$$L = R + G + B, \quad (1)$$

$$a = \frac{R - G}{L}, \quad (2)$$

$$b = \frac{R + G - 2B}{L}, \quad (3)$$

All RGB pixel values of processed images are previously corrected with $\gamma = 1/2.2$.

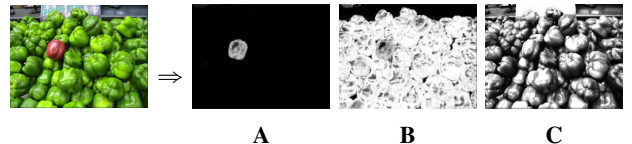


Fig. 2: Example of RGB image (top row) after converting the RGB values to the Lab color space (bottom row), correspondingly to color opponencies (A) “red vs green” (a^*), (B) “blue vs yellow” (b^*) and (C) “brightness” (L^*).

2) *Multiscale and orientation representation:* V1 cell sensitivities to distinct orientations [31] and spatial frequencies [46] are usually modeled as Gabor filters. Since Gabor transforms cannot be inverted to obtain the original image, we used the *à trous* algorithm, which is an undecimated discrete wavelet transform (DWT) [26][71, Chapter 6]. This decomposition allows to perform an inverse, where the basis functions remain similar to Gabor filters. We propose biologically plausible computations for extracting multiple orientations and multi-scale feature representations of from V1’s receptive field (RF) hypercolumnar organization (Fig. 3). The wavelet approximation planes $c_{s,\theta}$ (s for scale and θ for orientation) are computed by convolving the image with the filter h_s .

$$\begin{aligned} c_{s,h} &= c_{s-1} \otimes h_s, \\ c_{s,v} &= c_{s-1} \otimes h'_s. \end{aligned} \quad (4)$$

The filter h_s is obtained from h_{s-1} by doubling its size, i.e. $h_s = \uparrow h_{s-1}$, where \uparrow means upsampling by introducing zeros between the coefficients. The filter (h_s) for the first scale is

$$h_1 = \frac{1}{16} [1 \quad 4 \quad 6 \quad 4 \quad 1]$$

This filter can be also transposed (h'_s) to obtain distinct approximation orientation planes $c_{s,h}$ and $c_{s,v}$. From these approximation planes, we can obtain the wavelet coefficients $\omega_{s,\theta}$ at distinct scales and orientations:

$$\begin{aligned} \omega_{s,h} &= c_{s-1} - c_{s,h}, \\ \omega_{s,v} &= c_{s-1} - c_{s,v}, \\ \omega_{s,d} &= c_{s-1} - (c_{s,h} \otimes h'_s + \omega_{s,h} + \omega_{s,v}), \\ c_s &= c_{s-1} - (\omega_{s,h} + \omega_{s,v} + \omega_{s,d}). \end{aligned} \quad (5)$$

Here, ω_h , ω_v and ω_d correspond to the coefficients with ‘‘horizontal’’, ‘‘vertical’’ and ‘‘diagonal’’ orientations. Initial $c_0 = I_o$ is obtained from the CIE $L^*a^*b^*$ components ($o = L^*, a^*, b^*$) and c_n corresponds to the residual plane of the last wavelet component (e.g. $s = n$). The inverse transform is obtained by integrating wavelet coefficients and residual planes:

$$I'_o = \sum_{s=1, \theta=h,v,d}^n \omega_{s,\theta} + c_n. \quad (6)$$

Considering that for every image, $M \times N$ is the size of the feature map (resized to $N \leq 256$), wavelet coefficient scales are defined to model the spatial frequency sensitivities ($s = 1..S$), where $S = \log_2(N/16) + 1$.

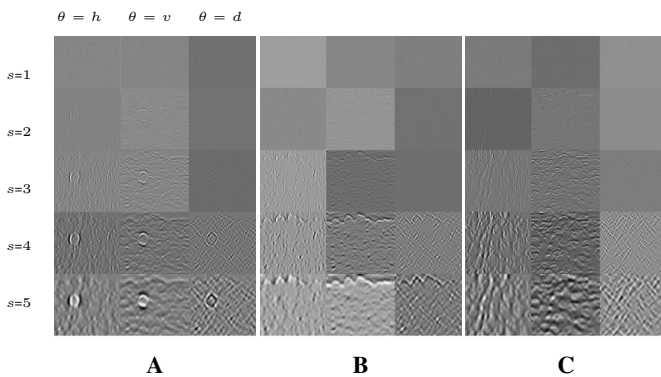


Fig. 3: Output from \hat{a} -trous DWT of the signals shown on Fig. 2. We show values for rescaled wavelet filters, with scales $s = 1..5$ and orientations $\theta = h, v, d$ corresponding to distinct channel opponencies (A) $\omega_{o=a^*}$, (B) $\omega_{o=b^*}$ and (C) $\omega_{o=L^*}$.

B. Computing V1 Dynamics: Feature Conspicuity

Feature conspicuity from previous Murray’s SWAM model is computed using center-surround feature computations while applying a contrast sensitivity function. Similarly, we extract

low-level feature-dependent computations corresponding to the orientation sensitivities ($\theta = 0, 90, 45/135$) of the respective retinotopic positions (i) at distinct spatial frequencies (s) for ON and OFF-center cells, but feature distinctiveness is computed with a network of firing rate neurons (FNN), simulating V1’s lateral interactions (Fig. 4). Contrast enhancement or suppression emerges from lateral connections as an induction mechanism.

Lateral interactions are implemented to have self-directed (J_0) and monosynaptic connections (J) between excitatory neurons. Inhibitory interactions have dysynaptic connections (W) through all inhibitory interneurons, defined by:

$$J_{[is\theta, js'\theta']} = \lambda(\Delta_s)0.126e^{(-\beta/d_s)^2 - 2(\beta/d_s)^7 - d_s^2/90}, \quad (7)$$

$$W_{[is\theta, js'\theta']} = \lambda(\Delta_s)0.14(1 - e^{-0.4(\beta/d_s)^{1.5}})e^{(\Delta_\theta/(\pi/4))^{1.5}}, \quad (8)$$

The aforementioned connections in (Eqs. 7,8) are defined by a concentric toroid of radius $\Delta_s = 15 \times 2^{s-1}$ and radial distance Δ_θ (respectively accounting for the distance between RF neurons from different spatial frequencies as d_s and radial distance as β) for the projections of these receptive fields.

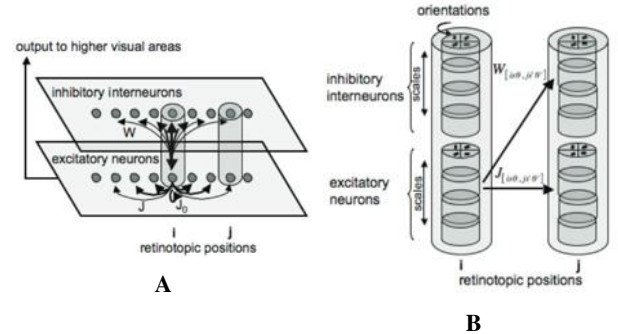


Fig. 4: Illustration of the receptive field properties of the network (A) and columnar organization of V1 excitatory and inhibitory interneurons (B). Reprinted with permission from ‘‘A Neurodynamical Model of Brightness Induction in V1’’, 2013, by O. Penacchio, *PLoS ONE*, 8(5):e64086, p.5. Copyright 2013 by the Public Library of Science [58].

Excitatory and inhibitory membrane potentials (their derivatives) are described by

$$\begin{aligned} \dot{x}_{is\theta} &= -\alpha_x x_{is\theta} - g_y(y_{is\theta}) \\ &\quad - \sum_{\Delta_s, \Delta_\theta \neq 0} \Psi(\Delta_s, \Delta_\theta) g_y(y_{is} + \Delta_{s\theta} + \Delta_\theta) + J_0 g(x_{is\theta}) \\ &\quad + \sum_{j \neq i, s', \theta'} J_{[is\theta, js'\theta']} g_x(x_{js'\theta'}) + I_{is\theta} + I_0, \end{aligned} \quad (9)$$

$$\begin{aligned} \dot{y}_{is\theta} &= -\alpha_y y_{is\theta} - g_x(x_{is\theta}) \\ &\quad + \sum_{j \neq i, s', \theta'} W_{[is\theta, js'\theta']} g_x(x_{js'\theta'}) + I_c. \end{aligned} \quad (10)$$

Functions g_x and g_y correspond to the activation function (implemented as piece-wise linear functions) for transforming the membrane potentials to firing rate values. The spread of the inhibitory activity within a hypercolumn is represented as Ψ , and α_x, α_y are constants for modulating the excitatory and inhibitory potentials. The variable $I_{is\theta}$ corresponds to the

external input values of the image ($I_{is\theta} \equiv \omega_{is\theta}$). Inhibitory top-down activity can be introduced to the model through I_c , but we defined it to uniquely have a gaussian noise signal (to stabilize the nonlinear equilibrium). Further details of the model and its parameters are specified in [58, Supporting Information S1].

We compute the temporal average of ON and OFF-center cells $M(\omega_{is}^{t+})$ and $M(\omega_{is}^{t-})$ as the model output over several oscillation cycles (being the mean of g_x for a specific range of t , where t is the membrane time, which corresponds to 10 ms) from distinct color opponencies ($o = L^*, a^*, b^*$). Distinctively from the induction cases described in Reproducing other visual effects, we do not combine the model output $M(\omega_{iso}^t)$ to the coefficients ω_{iso}^t , instead, we consider the firing rate from the model output as our predictor of feature distinctiveness, which will define our main function for our saliency map (Eq. 11). The model output can provide detail of single neuron dynamics of firing rate, which its dynamical properties may vary across stimulus properties from dimensions of color opponency, scale and orientation.

$$\hat{S}_{i;o}^t = \sum_{s=1..S; \theta=h;d;v;d}^{n_s} M(\omega_{iso\theta}^{t+}) + \sum_{s=1..S; \theta=h;d;v;d}^{n_s} M(\omega_{iso\theta}^{t-}) + c_i, \quad (11)$$

C. Generating the saliency map: Feature Integration

After computing feature distinctiveness for the low-level feature maps, we need to integrate these conspicuity or distinctiveness maps in order to pool the neuronal activity to the projections of the SC as means of acquiring a unique map, which will represent our saliency map. First, we have computed the inverse transform from the DWT (IDWT) Eq. 6 for integrating the sensitivities for orientation (θ) and spatial frequencies (s). Second, we have computed the euclidean norm (\hat{S}) for integrating the firing rate of the distinct color opponencies (Eq. 12). Third, we have normalized the resulting map ($z(\hat{S})$) by the variance of the firing rate (Eq. 13), as stated by Li [87, Chapter 5]. Finally, we convolved the saliency map with a gaussian filter in order to simulate a smoothing caused by the deviations of $\sigma = 1$ deg given from eye tracking experimentation, recommended by LeMeur & Baccino [40].

$$\hat{S}_i = \sqrt{\hat{S}_{i;a^*} + \hat{S}_{i;b^*} + \hat{S}_{i;L^*}}, \quad (12)$$

$$z_i(\hat{S}) = \frac{\hat{S}_i - \mu_{\hat{S}}}{\sigma_{\hat{S}}}, \quad (13)$$

III. EXPERIMENTS

Fixations and saccades are captured using eye-tracking technology. Eye movement data is combined across all fixations from participants' data, being represented as binary maps (called fixation maps), according to the fixation localizations in the visual space for each corresponding image, or as density distributions (alternatively named density maps) from these

fixations considering eye-movement localization probabilities (Figure 6). Fixation density maps are computed accordingly from fixation maps with a gaussian filter [40].

Prediction scores are calculated using spatially-dependent metrics [14][13] which compare either fixation maps or fixation density maps to saliency map predictions from the models (AUC, CC, NSS, KL and SIM). Essentially, these metrics assign a score considering true positive values for the saliency predictions inside the locations from the fixation maps (or higher correlations with respect to density maps) and false positive values for the reverse cases. Other metrics (sAUC) also consider false positive values by comparing the saliency maps with a baseline set of other image fixation maps in order to prevent behavioral tendencies such as center biases, which are not representative data for saliency prediction. Similarly, a baseline of several random images is used (InfoGain) for minimizing dataset center biases on prediction scores.

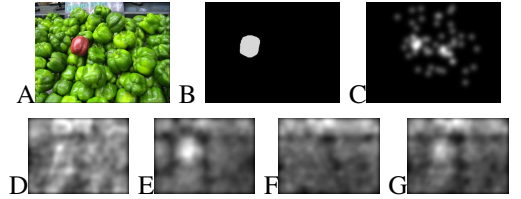


Fig. 5: (A) Example Image. (B) Mask of salient region. (C) Fixation density map (GT). (D,E,F,G) Predicted saliency map given $z(\hat{S}_{i;L^*})$, $z(\hat{S}_{i;a^*})$, $z(\hat{S}_{i;b^*})$ and $z(\hat{S}_i)$ respectively. (E) Results of prediction metrics from these saliency maps. $z(\hat{S})$ corresponds to our model's saliency prediction (NSWAM) used in our experiments.

A. Predicting human eye movements

We have computed the saliency maps² for images from distinct eye-tracking datasets, corresponding to 120 real scenes (Toronto) [10], 40 nature scenes (KTH) [36], 100 synthetic patterns (CAT2000_{Pattern})[6] and 230 synthetic images with specific feature contrast (SID4VAM) [3]. We have computed these image datasets with deep supervised artificial saliency models that specifically compute high-level features (OpenSali-con [30][73], DeepGazeII [37], SAM [17], SalGan [56]), and models that extract low-level features, corresponding to the

²Code for model evaluations can be downloaded from <https://github.com/dberga/saliency>

cases with artificial (SUN [86], GBVS [28]) and biological inspiration (IKN [33], AIM [11], SSR [68], AWS [25] and SWAM [48]).

	method	↑AUC _{Judd}	↑AUC _{Borji}	↑CC	↑NSS	↑KL	↑SIM	↑sAUC	↑InfoGain
HIGH-LEVEL	Humans	0.969	0.954	1.000	3.831	0.000	1.000	0.903	2.425
	OpenSalicon	0.821	0.771	0.522	1.655	1.113	0.429	0.716	0.232
	DeepGazell	0.850	0.768	0.595	1.877	0.997	0.483	0.717	0.422
	SAM _{RESNET}	0.850	0.725	0.612	1.955	2.420	0.516	0.666	-1.555
	SAM _{VGG}	0.569	0.543	0.055	0.158	11.972	0.214	0.506	-15.522
	SalGan	0.858	0.816	0.629	1.898	0.986	0.510	0.716	0.387
LOW-LEVEL	SUN	0.694	0.682	0.242	0.755	1.589	0.290	0.645	-0.499
	GBVS	0.817	0.803	0.487	1.431	1.168	0.397	0.632	0.077
	SSR	0.765	0.756	0.364	1.084	1.355	0.340	0.700	-0.174
	AWS	0.773	0.761	0.401	1.229	1.322	0.352	0.714	-0.106
	AIM	0.727	0.716	0.292	0.883	1.612	0.314	0.663	-0.580
	IKN	0.794	0.782	0.421	1.246	1.248	0.366	0.650	-0.024
	SWAM	0.754	0.744	0.317	0.951	1.486	0.302	0.705	-0.369
	NSWAM (Ours)	0.706	0.694	0.257	0.764	1.604	0.278	0.631	-0.552

TABLE I: Results for prediction metrics with Toronto dataset [11], corresponding to real (indoor and outdoor) images.

	method	↑AUC _{Judd}	↑AUC _{Borji}	↑CC	↑NSS	↑KL	↑SIM	↑sAUC	↑InfoGain
HIGH-LEVEL	Humans	0.902	0.850	1.000	2.038	0.000	1.000	0.822	1.415
	OpenSalicon	0.634	0.611	0.300	0.452	0.780	0.541	0.556	-0.278
	DeepGazell	0.648	0.618	0.362	0.578	0.678	0.559	0.588	-0.104
	SAM _{RESNET}	0.660	0.599	0.371	0.570	3.125	0.508	0.548	-3.643
	SAM _{VGG}	0.525	0.525	0.058	0.074	8.800	0.354	0.501	-11.836
	SalGan	0.655	0.626	0.391	0.581	1.666	0.544	0.560	-1.554
LOW-LEVEL	SUN	0.535	0.532	0.083	0.132	0.804	0.512	0.526	-0.303
	GBVS	0.649	0.638	0.351	0.505	0.711	0.563	0.533	-0.177
	SSR	0.575	0.573	0.172	0.270	0.778	0.525	0.557	-0.260
	AWS	0.587	0.583	0.210	0.329	0.851	0.511	0.581	-0.362
	AIM	0.572	0.568	0.179	0.274	0.918	0.523	0.552	-0.509
	IKN	0.617	0.611	0.274	0.403	0.714	0.547	0.551	-0.173
	SWAM	0.587	0.584	0.201	0.311	0.745	0.531	0.573	-0.212
	NSWAM (Ours)	0.598	0.593	0.230	0.345	0.711	0.536	0.565	-0.168

TABLE II: Results for prediction metrics with KTH dataset [36] subset of uniquely nature images.

	method	↑AUC _{Judd}	↑AUC _{Borji}	↑CC	↑NSS	↑KL	↑SIM	↑sAUC	↑InfoGain
HIGH-LEVEL	Humans	0.895	0.826	0.890	2.335	0.265	0.736	0.623	0.777
	OpenSalicon	0.651	0.621	0.220	0.603	1.526	0.357	0.555	-1.092
	DeepGazell	0.611	0.561	0.157	0.467	1.932	0.325	0.547	-1.657
	SAM _{RESNET}	0.766	0.711	0.518	1.356	1.747	0.456	0.546	-1.444
	SAM _{VGG}	0.625	0.581	0.123	0.320	8.581	0.322	0.508	-11.262
	SalGan	0.751	0.714	0.417	1.080	1.720	0.430	0.553	-1.384
LOW-LEVEL	SUN	0.549	0.539	0.068	0.193	5.860	0.280	0.526	-7.237
	GBVS	0.759	0.717	0.399	1.056	1.113	0.430	0.561	-0.503
	SSR	0.592	0.582	0.118	0.318	1.760	0.334	0.568	-1.432
	AWS	0.604	0.594	0.209	0.609	1.521	0.339	0.595	-1.077
	AIM	0.570	0.565	0.118	0.332	5.323	0.301	0.544	-6.490
	IKN	0.701	0.692	0.323	0.828	1.267	0.382	0.562	-0.724
	SWAM	0.586	0.578	0.120	0.336	1.614	0.328	0.566	-1.225
	NSWAM (Ours)	0.588	0.584	0.139	0.383	1.471	0.326	0.571	-1.017

TABLE III: Results for prediction metrics with CAT2000 dataset [6] training subset (Pattern) of uniquely synthetic images.

	method	↑AUC _{Judd}	↑AUC _{Borji}	↑CC	↑NSS	↑KL	↑SIM	↑sAUC	↑InfoGain
HIGH-LEVEL	Humans	0.943	0.882	1.000	4.204	0.000	1.000	0.860	2.802
	OpenSalicon	0.692	0.673	0.284	0.956	1.549	0.375	0.615	0.052
	DeepGazell	0.640	0.634	0.177	0.630	1.685	0.336	0.618	-0.150
	SAM _{RESNET}	0.727	0.673	0.305	0.967	2.610	0.388	0.600	-1.475
	SAM _{VGG}	0.537	0.523	0.026	0.070	11.947	0.216	0.503	-14.954
	SalGan	0.715	0.662	0.287	0.883	2.506	0.373	0.593	-1.350
LOW-LEVEL	SUN	0.542	0.532	0.080	0.333	16.408	0.165	0.530	-21.024
	GBVS	0.747	0.718	0.400	1.464	1.363	0.413	0.628	0.331
	SSR	0.672	0.665	0.192	0.639	1.904	0.365	0.642	-0.467
	AWS	0.679	0.667	0.255	1.088	1.592	0.373	0.672	0.013
	AIM	0.570	0.566	0.122	0.473	14.472	0.224	0.557	-18.182
	IKN	0.686	0.678	0.283	0.878	1.748	0.380	0.608	-0.233
	SWAM	0.650	0.641	0.189	0.694	1.702	0.357	0.619	-0.148
	NSWAM (Ours)	0.614	0.610	0.136	0.529	1.686	0.335	0.622	-0.150

TABLE IV: Results for prediction metrics with SID4VAM dataset [3] with synthetic images.

Our results show that our model has a trend to acquire other saliency models performance, with an emphasis on

outperforming previous Murray’s SWAM model for the cases of KTH, CAT2000 and SID4VAM (Tables II, III and IV), corresponding to nature and synthetic images, as well as showing stable metric scores for distinct contexts (similarly as AWS and GBVS). NSWAM outperforms other biologically-inspired models (IKN, AIM, SSR & SWAM) specially for metrics that account for center biases. These center biases are qualitatively present even for images where the salient region is conspicuous Fig. 6, rows 5 & 6. Saliency models that compute high-level visual features are shown to perform better with real image scenes (Table I). However, the image contexts that lack of high-level visual information should be more representative indicators of saliency, due to the absence of semantically or contextually-relevant visual information (nature images), or to be characterized to uniquely contain low-level features (synthetic images) presenting clear pop-out spots to direct participants fixations (which would cause lower inter-participant differences and therefore lower center biases). Although AWS and GBVS perform better on predicting fixations at distinct contexts, we remark the plausibility of our unified design for modeling distinct HVS’ functionality. NSWAM shows a new insight of applying a more biologically plausible computation of the aforementioned steps. First, we transform image values to color opponencies, found in RGC. Second, we model LGN projections to V1 simple cells using a multiresolution wavelet transform. Third, conspicuity is computed with a dynamical model of the lateral interactions of V1. Fourth, these channels are integrated to a unique map which will represent SC activity. Using a neurodynamic model with firing-rate neurons allows a more detailed understanding of the dependency of saliency on lateral connections and a potential further study in terms of single neuron dynamics using real image scenes.

B. Psychophysical measurements

Acknowledging that the HVS processes information according to the context, human performance on detecting a salient object on a scene may also vary according to the visual properties of such object. With a synthetic image dataset [3] a specific analysis of how each individual feature influences saliency can be done. In this study we will show how fixation data is predicted when varying feature contrast, concretely on parametrizing Set Size, and Brightness, Color, Size and Orientation contrast between a target salient object Fig. 5B and the rest of distractors (feature singleton search). In this section a set of psychophysical stimuli will be displayed with its parametrization of set size or feature contrast and its SI in comparison to other biologically-inspired saliency models.

Saliency Index (SI) [3][69][70] is another measurement for saliency evaluation (Eq. 14). It calculates of the energy of the fixation density map inside (S_t) a salient region (which would enclose a salient object, as in Fig. 5B) compared to the energy outside (S_b) the salient region.

$$SI(S_t, S_b) = \frac{S_t - S_b}{S_b}. \quad (14)$$

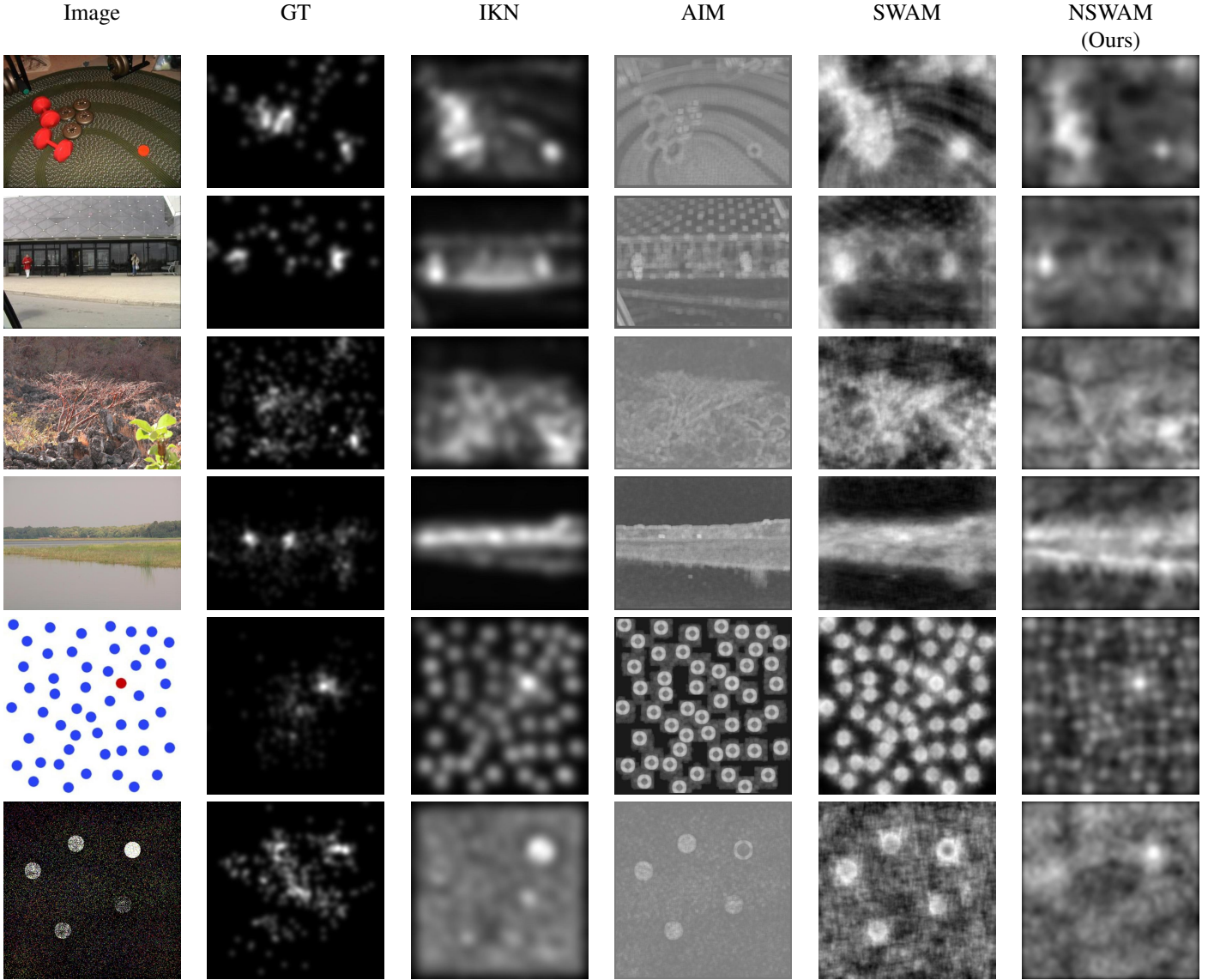


Fig. 6: Examples of saliency maps from the models Itti et al. (IKN), Bruce & Tsotsos (AIM), Murray et al. (SWAM) and our model (columns 3 to 6, respectively), corresponding to images with distinct contexts (first column). We also show the density distribution of fixations given by the eye-tracking experimentation (second column).

1) *Brightness differences*: Differences in brightness are major factors for making an object to attract attention. Thus, a bright object is less salient as luminance of other objects increase (Fig. 7). Conversely, a dark target in a bright background will be more salient as distractors have higher luminance [57][53]. NSWAM processes luminance signals separately from chromatic ones using the L^* channel (feature conspicuity from a distinctively bright object upon a dark background will be processed similarly to a dark object upon a bright background). We compare SI metrics for both conditions and NSWAM is shown to acquire similar performance to SWAM, with higher SI than IKN Fig. 8,A-B, specially for stimulus with higher contrasts ($\Delta L_{D,T} > .25$). Results on SI for NSWAM correlates with brightness contrast, for both cases of bright ($\rho = .941, p = 1.6 \times 10^{-3}$) and dark ($\rho = .986, p = 4.7 \times 10^{-5}$) background.

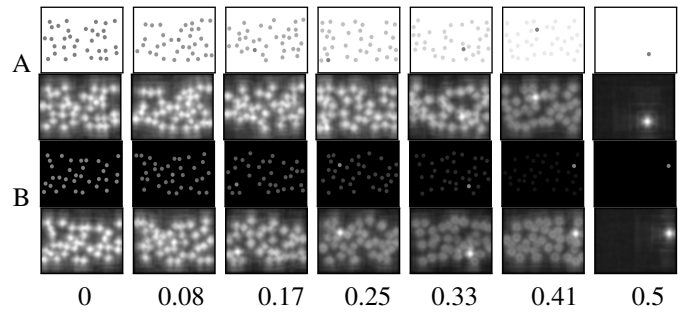


Fig. 7: Array of synthetic stimuli representing distinct brightness contrasts (HSL luminance differences) from target and distractors ($\Delta L_{D,T}$) with (A) bright background ($L_T = 0.5, L_B = 1, L_D = 0.5..1$) and conversely, with (B) dark background ($L_T = 0.5, L_B = 0, L_D = 0..0.5$). Rows below A,B correspond to NSWAM’s predicted saliency maps.

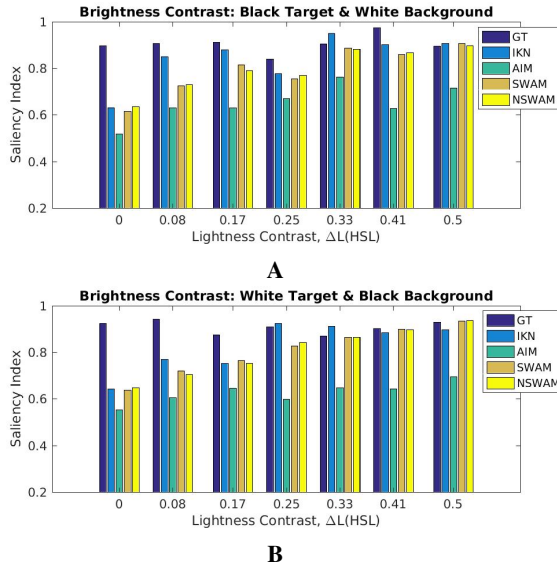


Fig. 8: Results of SI upon brightness contrast on a luminance singleton ($\Delta L_{D,T}$) with a (A) bright and (B) dark background.

2) *Color differences*: Color changes spatial and temporal behavior of eye movements, influencing how conspicuous are specific objects on a scene [21][2]. Similarly to previous section, here we vary the chromaticity of the background, which can alter search efficiency [49][18]. In this section, we used stimuli similar to Rosenholtz’s experimentation [64], with red and blue singletons for achromatic or oversaturated backgrounds Fig. 9. Here, chromatic contrast is defined as the HSL saturation differences ($\Delta S_{D,T}$) between a salient target and the rest of distractors.

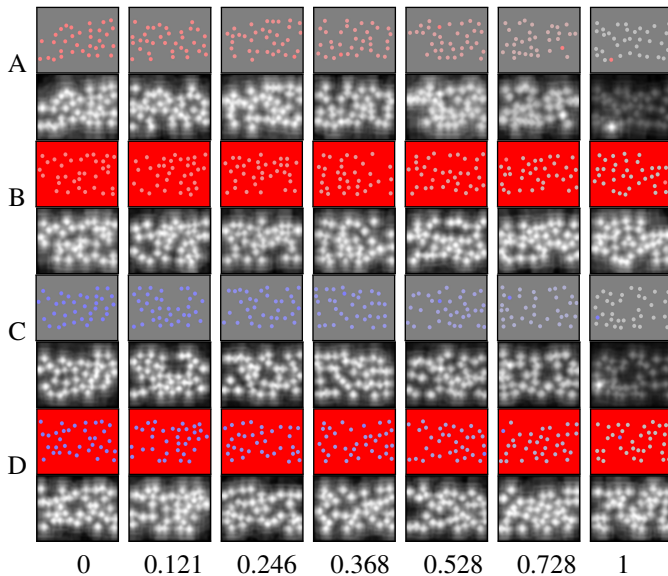


Fig. 9: Chromatic stimuli representing saturation contrast ($\Delta S_{D,T}$) between a red target ($H_T = 0$) and an (A) unsaturated, grey background or an (B) oversaturated, red background. Other cases (C,D) present a blue target ($H_T = 240$) with same background properties to (A) and (B) respectively. Rows below A-D correspond to NSWAM’s predicted saliency maps.

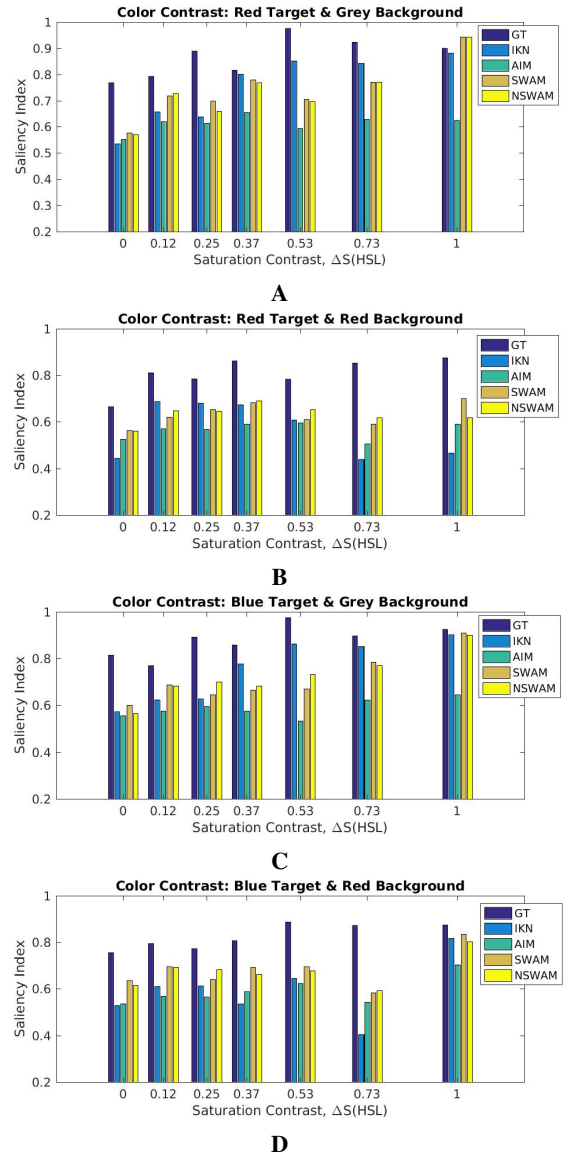


Fig. 10: Results of SI upon saturation contrast ($\Delta S_{D,T}$) on a red singleton with (A) achromatic or (B) oversaturated red background, or either a blue singleton with (C) achromatic or (D) oversaturated red background.

Similarly to Fig. 7, NSWAM has similar SI to SWAM for all background conditions (Fig. 10,A-D). Achromatic backgrounds contribute to salient object detection by increasing SI of the pop-out singleton. That effect is present for visual search results and our saliency prediction. Results comparing target search fixation maps and SI show distinct performance upon saturation contrast depending on background conditions. Cases which stimulus background was achromatic, distinct from the feature singleton, had higher correlation than with oversaturated background. For the cases of grey (achromatic) background, there is a correlation between SI results for our model and $\Delta S_{D,T}$ with a red ($\rho = .864, p = 1.2 \times 10^{-2}$) and blue ($\rho = .944, p = 1.4 \times 10^{-3}$) target singleton. However, when background color is oversaturated red and targets are either red ($\rho = .106, p = .82$) or blue ($\rho = .483, p = .27$), then saturation contrast do not correlate with SI.

3) *Size contrast*: Feature distinctiveness with feature singletons have been tested by varying set size, object orientation and/or color. Here we will test how object size affects its saliency, previously tested with visual search experimentation [27][72][61]. A set of 34 symmetric objects (with a dark circle shape) are distributed randomly around the image Fig. 11, preserving equal diameter. One of the circles is defined with dissimilar size, either with higher or lower diameter with respect the rest of distractors (which are defined with a diameter of 2.5 deg). Performance for NSWAM’s SI improves with object size dissimilarity. We can observe that when the diameter of the dissimilar circle is higher, SI is higher for that particular region. For the highest scaling factor (when the dissimilar object is bigger), NSWAM has higher SI compared to previous biologically-inspired models (Fig. 12). Plus, there is a significant correlation between circle diameter and our model’s results of SI ($\rho = .955, p = 8.3 \times 10^{-4}$).

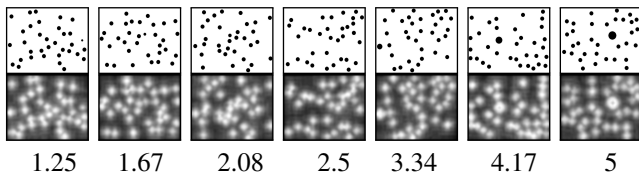


Fig. 11: Examples of circle distractors with equal diameter ($\varnothing_D=2.5\text{deg}$), containing a salient one with dissimilar size ($\varnothing_T=1.25..5\text{deg}$) with respect the rest. In lower row there are NSWAM’s predicted saliency maps.

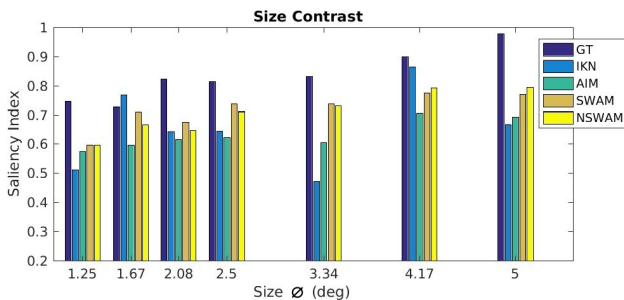


Fig. 12: SI results for Size Contrast stimuli.

4) *Orientation contrast*: Using a similar setting, varying angle of objects is found to increase search efficiency when angle contrast is increased [20][52][51]. A total of 34 bars were oriented horizontally and randomly displaced around the scene (Fig. 13). The dissimilar object for this case is a bar oriented with an angle contrast with respect the rest of bars of $\Delta\Phi(1,0)=[0, 10, 20, 30, 42, 56, 90]$. Although results of SI show that NSWAM overperforms SWAM’s saliency maps, IKN is best for capturing orientation distinctiveness (Fig. 14). In NSWAM, 3 types of orientation selective cells are modeled, corresponding to the orientation for the wavelet coefficients ($\theta = h, v, d$). A higher number of orientation selective cells would provide a higher accuracy, specially for diagonal angles (here we only provide $\theta = d$ for 45/135 combined). By modeling orientation selective cells with 2D Gabor and Log-Gabor transforms [39][23][25] it would be

possible to correctly build an hypercolumnar organization with a higher number of angle sensitivities, adding detail to the proposed model. We have to acknowledge that for this experimentation, distractors have been set with same horizontal configuration. Specific connectivity interactions [1] between orientation dissimilarities needs to be defined in order to reproduce orientation-dependent visual illusions and conspicousness under heterogeneous, nonlinear and categorical angle configurations, which are previously known to distinctively affect visual attention [52][51][24].

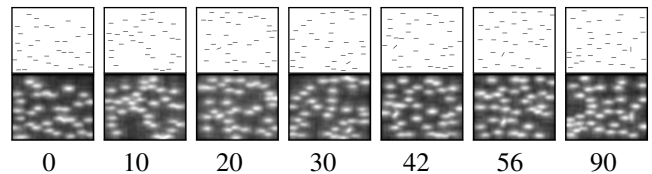


Fig. 13: An oriented bar with an orientation contrast of $\Delta\Phi = 0..90$ with respect to a set of bars oriented at $\Phi_D = 0$. In lower row there are NSWAM’s predicted saliency maps.

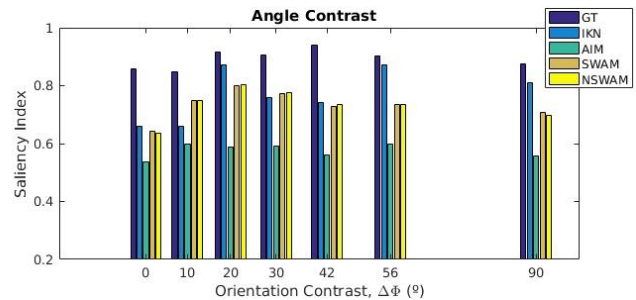


Fig. 14: SI results for Orientation Contrast stimuli.

5) *Visual Asymmetries*: Search asymmetries appear when searching target of type “a” is found efficiently among distractors of type “b”, but not in the opposite case (i.e. searching for “b” among distractors of type “a”) [74][83]. Previous studies pointed out this this concept when searching a circle crossed by a vertical bar among plain circles and searching a plain circle among circles crossed by a vertical bar). Using these two configurations, we filled a grid of distractors according to specific scales (Fig. 15). Scale values ($s = [1.25, 1.67, 2.08, 2.5, 3.33, 4.17, 5]$ deg) are defined in a way to change the amount of items to be presented, corresponding to arrays of $5 \times 7, 6 \times 8, 8 \times 10, 10 \times 13, 15 \times 20$ and 20×26 objects. In Fig. 8 we can see that our model is not only more efficient than other biologically-inspired models for predicting saliency upon dissimilar objects in size but also on detecting conspicuous objects at distinct scales, accounting for lower or larger amount of distractors. SI for NSWAM showed to correlate for a conspicuous circle crossed by a vertical bar among circles ($\rho = .83, p = 2.1 \times 10^{-2}$) but not for a conspicuous circle among circles crossed by a vertical bar ($\rho = .15, p = .75$).

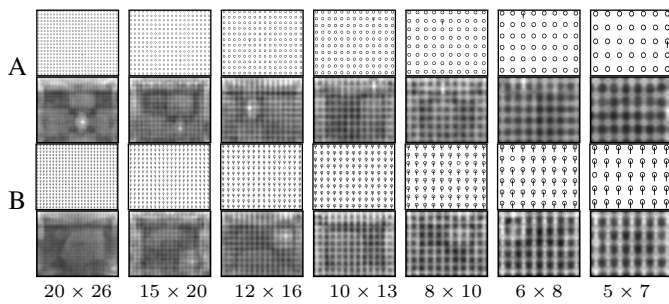


Fig. 15: Stimuli with distinct set sizes corresponding to search asymmetries present on a (A) salient circle crossed by a vertical bar among other circles and a (B) salient circle among other circles crossed by a vertical bar. Rows below A,B correspond to NSWAM’s predicted saliency maps.

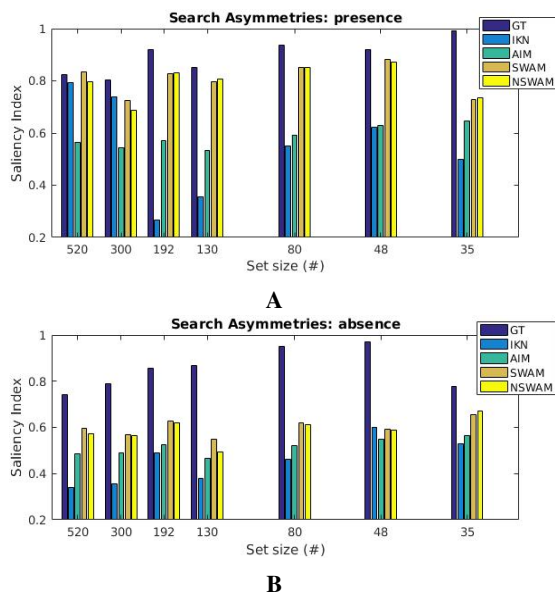


Fig. 16: Results of SI upon varying scale and set size of (A) an array of circles and a salient one crossed by a vertical bar and (B) an array of circles crossed by a bar and a salient circle.

IV. CONCLUSION

In this work, we hypothesize that low-level saliency is likely to be associated by the computations of V1. For such, we proposed a neurodynamic model of V1’s lateral interactions, processing each channel separately and acquiring firing rate dynamics from real image simulations. Here we have to pinpoint three statements in agreement with our findings:

- First, our model has a trend to acquire state-of-the-art results on human eye fixations, specifically, with natural and synthetic images.
- Second, our model improves results for biologically-inspired saliency models and it is consistent with human psychophysical measurements (tested for Visual Asymmetries, Brightness, Color, Size and Orientation contrast). Adding up to the stated hypothesis, our model presents highest performance at highest contrast from feature singleton stimuli (where salient objects pop-out more easily).

- Three, we remark the model plausibility by mimicking HVS physiology on its processing steps and being able to reproduce other effects such as Brightness Induction [58], Color Induction [15] and Visual Discomfort [60], efficiently working without applying any type of training or optimization and keeping the same parametrization.

Other biologically plausible alternatives that predict attention using neurodynamic modeling [42][19][16] do not provide a unified model of the visual cortex able to reproduce these distinct tasks simultaneously, and specifically, using real static or dynamic images as input. We suggest that V1 computations work as a common substrate for several tasks simultaneously.

Future work of interest would consist on predicting scan-paths for real scenes in order to provide gaze-wise temporal detail for saliency prediction and saccade programming. To do so, a foveation mechanism (such as a retinal [78] or a cortical magnification transformation towards V1 retinotopy [67]) would be needed in order to process each view of the scene distinctively. Other applications of the same model would be to generate saliency maps with dynamic scenes or videos, integrating other features such as flicker or motion. In order to provide top-down computations for representing feature relevance apart from saliency, we could feed our model with a selective mechanism [75][29] for specific low-level feature maps, enabling the possibility to perform visual search tasks. Saliency computations could be more accurately represented with a higher number of 2D Gabor/Log-Gabor filters [39][23][25] as well as the specificities of intra and inter-cortical interactions between simple and complex cells in a multilayer implementation of V1. Such implementation could adequate more detailed and efficient computations of V1, projecting the excitatory recurrent dynamics from V1 (specifically from Layer 5 complex cells, also named “Meynert” cells) to SC [45][50].

Although latest hypotheses about the SC confirm that saliency is processed in the SC and not by the visual cortex, corresponding to a distinct, feature-agnostic saliency map [76][81], we claim the importance of the mechanisms of V1 to be responsible for computing distinctiveness between the stated low-level features, which might conjunctively contribute to the generation of saliency [43][44][84]. However, modeling the computations of the pathways from the RGC to the SC would be of interest for a more integrated and complete model of eye-movement prediction, seeing the roles of the distinct projections to the SC and their computations, alternatively involved in the control of eye movements.

REFERENCES

- [1] M. A. Asenov. Dynamic model of interactions between orientation selective neurons in primary visual cortex. Master’s thesis, University of Edinburgh, Edinburgh, UK, 2016.
- [2] B. Bauer, P. Jolicœur, and W. B. Cowan. Distractor heterogeneity versus linear separability in colour visual search. *Perception*, 25(11):1281–1293, nov 1996.
- [3] D. Berga, X. Fdez-Vidal, X. Otazu, V. Leboran, and X. Pardo. Psychophysical evaluation of individual low-level feature influences on visual attention. *Vision Research, In Review*, 2018.
- [4] F. W. Billmeyer. Color science: Concepts and methods, quantitative data and formulae, 2nd ed., by gunter wyszecki and w. s. stiles, john wiley and sons, new york, 1982, 950 pp. price: \$75.00. *Color Research & Application*, 8(4):262–263, 1983.

- [5] A. Borji and L. Itti. State-of-the-art in visual attention modeling. *IEEE Transactions on Pattern Analysis and Machine Intelligence*, 35(1):185–207, jan 2013.
- [6] A. Borji and L. Itti. Cat2000: A large scale fixation dataset for boosting saliency research. *CVPR 2015 workshop on "Future of Datasets"*, 2015. arXiv preprint arXiv:1505.03581.
- [7] A. Borji, D. N. Sihite, and L. Itti. Quantitative analysis of human-model agreement in visual saliency modeling: A comparative study. *IEEE Transactions on Image Processing*, 22(1):55–69, jan 2013.
- [8] A. Borji, H. R. Tavakoli, D. N. Sihite, and L. Itti. Analysis of scores, datasets, and models in visual saliency prediction. In *2013 IEEE International Conference on Computer Vision*. IEEE, dec 2013.
- [9] N. D. Bruce, C. Wloka, N. Frosst, S. Rahman, and J. K. Tsotsos. On computational modeling of visual saliency: Examining what's right, and what's left. *Vision Research*, 116:95–112, nov 2015.
- [10] N. D. B. Bruce and J. K. Tsotsos. Saliency based on information maximization. In *Proceedings of the 18th International Conference on Neural Information Processing Systems, NIPS'05*, pages 155–162, Cambridge, MA, USA, 2005. MIT Press.
- [11] N. D. B. Bruce and J. K. Tsotsos. Saliency, attention, and visual search: An information theoretic approach. *Journal of Vision*, 9(3):5–5, mar 2009.
- [12] Z. Bylinskii, E. DeGennaro, R. Rajalingham, H. Ruda, J. Zhang, and J. Tsotsos. Towards the quantitative evaluation of visual attention models. *Vision Research*, 116:258–268, nov 2015.
- [13] Z. Bylinskii, T. Judd, F. Durand, A. Oliva, and A. Torralba. Mit saliency benchmark. <http://saliency.mit.edu/>.
- [14] Z. Bylinskii, T. Judd, A. Oliva, A. Torralba, and F. Durand. What do different evaluation metrics tell us about saliency models?, 2016.
- [15] X. Cerda and X. Otazu. A Multi-Task Neurodynamical Model of Lateral Interactions in V1: Chromatic Induction. *39th European Conference of Visual Perception, PERCEPTION*, 45(2):51, 2016.
- [16] S. Chevallier, N. Cuperlier, and P. Gaussier. Efficient neural models for visual attention. In *Computer Vision and Graphics*, pages 257–264. Springer Berlin Heidelberg, 2010.
- [17] M. Cornia, L. Baraldi, G. Serra, and R. Cucchiara. Predicting human eye fixations via an lstm-based saliency attentive model, 2016.
- [18] M. V. Danilova and J. D. Mollon. Symmetries and asymmetries in chromatic discrimination. *Journal of the Optical Society of America A*, 31(4):A247, feb 2014.
- [19] G. Deco and E. T. Rolls. A neurodynamical cortical model of visual attention and invariant object recognition. *Vision Research*, 44(6):621–642, mar 2004.
- [20] J. Duncan and G. W. Humphreys. Visual search and stimulus similarity. *Psychological Review*, 96(3):433–458, 1989.
- [21] M. D'Zmura. Color in visual search. *Vision Research*, 31(6):951–966, jan 1991.
- [22] H. E. Egeth and S. Yantis. VISUAL ATTENTION: Control, representation, and time course. *Annual Review of Psychology*, 48(1):269–297, feb 1997.
- [23] S. Fischer, F. Šroubek, L. Perrinet, R. Redondo, and G. Cristóbal. Self-invertible 2d log-gabor wavelets. *International Journal of Computer Vision*, 75(2):231–246, jan 2007.
- [24] D. Gao. *A discriminant hypothesis for visual saliency: computational principles, biological plausibility and applications in computer vision*. PhD thesis, UC San Diego, 2008.
- [25] A. Garcia-Diaz, X. R. Fdez-Vidal, X. M. Pardo, and R. Dosi. Saliency from hierarchical adaptation through decorrelation and variance normalization. *Image and Vision Computing*, 30(1):51–64, jan 2012.
- [26] M. González-Audicana, X. Otazu, O. Fors, and A. Seco. Comparison between mallat's and the 'à trous' discrete wavelet transform based algorithms for the fusion of multispectral and panchromatic images. *International Journal of Remote Sensing*, 26(3):595–614, feb 2005.
- [27] P. Goolkasian. Size scaling and spatial factors in visual attention. *The American Journal of Psychology*, 110(3):397, 1997.
- [28] J. Harel, C. Koch, and P. Perona. Graph-based visual saliency. *Proc. Advances in Neural Information Processing Systems (NIPS 2007)*, 19:545–552, 2007.
- [29] L. Huang and H. Pashler. A boolean map theory of visual attention. *Psychological Review*, 114(3):599–631, 2007.
- [30] X. Huang, C. Shen, X. Boix, and Q. Zhao. SALICON: Reducing the semantic gap in saliency prediction by adapting deep neural networks. In *2015 IEEE International Conference on Computer Vision (ICCV)*. IEEE, dec 2015.
- [31] D. H. Hubel and T. N. Wiesel. Receptive fields and functional architecture of monkey striate cortex. *The Journal of Physiology*, 195(1):215–243, mar 1968.
- [32] L. Itti. Visual salience. *Scholarpedia*, 2(9):3327, 2007.
- [33] L. Itti, C. Koch, and E. Niebur. A model of saliency-based visual attention for rapid scene analysis. *IEEE Transactions on Pattern Analysis and Machine Intelligence*, 20(11):1254–1259, 1998.
- [34] T. Judd, F. Durand, and A. Torralba. A benchmark of computational models of saliency to predict human fixations. *CSAIL Technical Reports*, jan 2012.
- [35] C. Koch and S. Ullman. Shifts in selective visual attention: Towards the underlying neural circuitry. In *Matters of Intelligence*, pages 115–141. Springer Netherlands, 1987.
- [36] G. Kootstra, B. de Boer, and L. R. B. Schomaker. Predicting eye fixations on complex visual stimuli using local symmetry. *Cognitive Computation*, 3(1):223–240, jan 2011.
- [37] M. Kmmmerer, T. S. A. Wallis, and M. Bethge. Deepgaze ii: Reading fixations from deep features trained on object recognition, 2016.
- [38] A. T. Le, J. Payne, C. Clarke, M. A. Kelly, F. Prudenziati, E. Armsby, O. Penacchio, and A. J. Wilkins. Discomfort from urban scenes: Metabolic consequences. *Landscape and Urban Planning*, 160:61–68, apr 2017.
- [39] T. S. Lee. Image representation using 2d gabor wavelets. *IEEE Transactions on Pattern Analysis and Machine Intelligence*, 18(10):959–971, 1996.
- [40] O. LeMeur and T. Baccino. Methods for comparing scanpaths and saliency maps: strengths and weaknesses. *Behavior Research Methods*, 45(1):251–266, jul 2012.
- [41] P. Lennie, J. Krauskopf, and G. Sclar. Chromatic mechanisms in striate cortex of macaque. *The Journal of Neuroscience*, 10(2):649–669, feb 1990.
- [42] Z. Li. A neural model of contour integration in the primary visual cortex. *Neural Computation*, 10(4):903–940, may 1998.
- [43] Z. Li. Contextual influences in v1 as a basis for pop out and asymmetry in visual search. *Proceedings of the National Academy of Sciences*, 96(18):10530–10535, aug 1999.
- [44] Z. Li. A saliency map in primary visual cortex. *Trends in Cognitive Sciences*, 6(1):9–16, jan 2002.
- [45] J. S. Lund and R. G. Boothe. Interlaminar connections and pyramidal neuron organisation in the visual cortex, area 17, of the macaque monkey. *The Journal of Comparative Neurology*, 159(3):305–334, feb 1975.
- [46] L. Maffei and A. Fiorentini. The visual cortex as a spatial frequency analyser. *Vision Research*, 13(7):1255–1267, jul 1973.
- [47] P. Monnier and S. K. Shevell. Chromatic induction from s-cone patterns. *Vision Research*, 44(9):849–856, apr 2004.
- [48] N. Murray, M. Vanrell, X. Otazu, and C. A. Parraga. Saliency estimation using a non-parametric low-level vision model. In *CVPR 2011*. IEEE, jun 2011.
- [49] A. L. Nagy. Interactions between achromatic and chromatic mechanisms in visual search. *Vision Research*, 39(19):3253–3266, oct 1999.
- [50] H. L. Nhan and E. M. Callaway. Morphology of superior colliculus- and middle temporal area-projecting neurons in primate primary visual cortex. *The Journal of Comparative Neurology*, 520(1):5280, Nov 2011.
- [51] H.-C. Nothdurft. The conspicuousness of orientation and motion contrast. *Spatial Vision*, 7(4):341–363, jan 1993.
- [52] H.-C. Nothdurft. The role of features in preattentive vision: Comparison of orientation, motion and color cues. *Vision Research*, 33(14):1937–1958, sep 1993.
- [53] H.-C. Nothdurft. Saliency from feature contrast: additivity across dimensions. *Vision Research*, 40(10-12):1183–1201, jun 2000.
- [54] X. Otazu, C. A. Parraga, and M. Vanrell. Toward a unified chromatic induction model. *Journal of Vision*, 10(12):5–5, oct 2010.
- [55] X. Otazu, M. Vanrell, and C. A. Parraga. Multiresolution wavelet framework models brightness induction effects. *Vision Research*, 48(5):733–751, feb 2008.
- [56] J. Pan, C. Canton, K. McGuinness, N. E. O'Connor, J. Torres, E. Sayrol, and X. a. Giro-i Nieto. Salgan: Visual saliency prediction with generative adversarial networks. In *arXiv*, January 2017.
- [57] H. Pashler, K. Dobkins, and L. Huang. Is contrast just another feature for visual selective attention? *Vision Research*, 44(12):1403–1410, jun 2004.
- [58] O. Penacchio, X. Otazu, and L. Dempere-Marco. A neurodynamical model of brightness induction in v1. *PLoS ONE*, 8(5):e64086, may 2013.
- [59] O. Penacchio and A. J. Wilkins. Visual discomfort and the spatial distribution of fourier energy. *Vision Research*, 108:1–7, mar 2015.
- [60] O. Penacchio, A. J. Wilkins, X. Otazu, and J. M. Harris. Inhibitory function and its contribution to cortical hyperexcitability and visual discomfort as assessed by a computation model of cortical function. *39th*

European Conference of Visual Perception, PERCEPTION, 45(2):51, 2016.

- [61] M. J. Proulx. Size matters: Large objects capture attention in visual search. *PLoS ONE*, 5(12):e15293, dec 2010.
- [62] N. Riche, M. Duvinage, M. Mancas, B. Gosselin, and T. Dutoit. Saliency and human fixations: State-of-the-art and study of comparison metrics. In *2013 IEEE International Conference on Computer Vision*. IEEE, dec 2013.
- [63] N. Riche and M. Mancas. Bottom-up saliency models for still images: A practical review. In *From Human Attention to Computational Attention*, pages 141–175. Springer New York, 2016.
- [64] R. Rosenholtz, A. L. Nagy, and N. R. Bell. The effect of background color on asymmetries in color search. *Journal of Vision*, 4(3):9, mar 2004.
- [65] P. H. Schiller, M. Stryker, M. Cynader, and N. Berman. Response characteristics of single cells in the monkey superior colliculus following ablation or cooling of visual cortex. *Journal of Neurophysiology*, 37(1):181–194, jan 1974.
- [66] P. H. Schiller and E. J. Tehovnik. *Vision : from neurons to cognition*. Elsevier Science, Amsterdam New York, 2001.
- [67] E. L. Schwartz. Computational anatomy and functional architecture of striate cortex: A spatial mapping approach to perceptual coding. *Vision Research*, 20(8):645–669, jan 1980.
- [68] H. J. Seo and P. Milanfar. Static and space-time visual saliency detection by self-resemblance. *Journal of Vision*, 9(12):15–15, nov 2009.
- [69] A. Soltani and C. Koch. Visual saliency computations: Mechanisms, constraints, and the effect of feedback. *Journal of Neuroscience*, 30(38):12831–12843, sep 2010.
- [70] M. Spratling. Predictive coding as a model of the v1 saliency map hypothesis. *Neural Networks*, 26:7–28, feb 2012.
- [71] T. Stathaki. *Image fusion : algorithms and applications*. Academic Press/Elsevier, Amsterdam Boston, 2008.
- [72] A. Tavassoli, I. van der Linde, A. Bovik, and L. Cormack. Eye movements selective for spatial frequency and orientation during active visual search. *Vision Research*, 49(2):173–181, jan 2009.
- [73] C. L. Thomas. Opensalicon: An open source implementation of the salicon saliency model. Technical Report TR-2016-02, University of Pittsburgh, 2016.
- [74] A. Treisman and J. Souther. Search asymmetry: A diagnostic for preattentive processing of separable features. *Journal of Experimental Psychology: General*, 114(3):285–310, 1985.
- [75] J. K. Tsotsos, S. M. Culhane, W. Y. K. Wai, Y. Lai, N. Davis, and F. Nuflo. Modeling visual attention via selective tuning. *Artificial Intelligence*, 78(1-2):507–545, oct 1995.
- [76] R. Veale, Z. M. Hafed, and M. Yoshida. How is visual salience computed in the brain? insights from behaviour, neurobiology and modelling. *Philosophical Transactions of the Royal Society B: Biological Sciences*, 372(1714):20160113, jan 2017.
- [77] N. Wade. *The art and science of visual illusions*. Routledge & Kegan Paul, London Boston, 1982.
- [78] A. B. Watson. A formula for human retinal ganglion cell receptive field density as a function of visual field location. *Journal of Vision*, 14(7):15–15, jun 2014.
- [79] B. White and D. P. Munoz. *The Oxford Handbook of Eye Movements*. Oxford University Press, aug 2011.
- [80] B. J. White, D. J. Berg, J. Y. Kan, R. A. Marino, L. Itti, and D. P. Munoz. Superior colliculus neurons encode a visual saliency map during free viewing of natural dynamic video. *Nature Communications*, 8:14263, jan 2017.
- [81] B. J. White, J. Y. Kan, R. Levy, L. Itti, and D. P. Munoz. Superior colliculus encodes visual saliency before the primary visual cortex. *Proceedings of the National Academy of Sciences*, 114(35):9451–9456, aug 2017.
- [82] M. White. A new effect of pattern on perceived lightness. *Perception*, 8(4):413–416, aug 1979.
- [83] J. M. Wolfe. Asymmetries in visual search: An introduction. *Perception & Psychophysics*, 63(3):381–389, apr 2001.
- [84] Y. Yan, L. Zhaoping, and W. Li. Bottom-up saliency and top-down learning in the primary visual cortex of monkeys. *Proceedings of the National Academy of Sciences*, page 201803854, sep 2018.
- [85] L. Zhang and W. Li. *Selective Visual Attention*. John Wiley & Sons (Asia) Pte Ltd, mar 2013.
- [86] L. Zhang, M. H. Tong, T. K. Marks, H. Shan, and G. W. Cottrell. SUN: A bayesian framework for saliency using natural statistics. *Journal of Vision*, 8(7):32, dec 2008.
- [87] L. Zhaoping. *Understanding vision : theory, models, and data*. Oxford University Press, Oxford, United Kingdom, 2014.



David Berga received his B.Sc. degree in Computer Science from Universitat Pompeu Fabra in 2014, where he received his M.Sc. degree in Cognitive Systems and Interactive Media in 2015. He is currently a researcher at the Computer Vision Center and a Ph.D. candidate with the Department of Computer Science at Universitat Autònoma de Barcelona, focused in modelling computational architectures of visual attention. His research interests are in the areas of Computational Neuroscience, Image Processing, Visual Perception and Psychophysics.



Xavier Otazu is an Associate Professor at the Department of Computer Science of Universitat Autònoma de Barcelona, and Senior Scientist at the Computer Vision Center. He received his B.Sc. in Physics, M.Sc. in Remote Sensing and Ph.D. in Physics (Astronomy Department) at Universitat de Barcelona where he worked on Astronomy and Remote Sensing data and image processing. He is currently working in the development of biologically plausible computational neurodynamic models of the visual cortex.